Research Square

Preprints are preliminary reports that have not undergone peer review.
They should not be considered conclusive, used to inform clinical practice,
or referenced by the media as validated information.

Gut Commensal Candida albicans Constrains Whole-Body Energy Storage in Mice

Marie-Claire Arrieta

marie.arrieta@ucalgary.ca

Department of Physiology and Pharmacology, University of Calgary, Calgary, AB, Canada.
https://orcid.org/0000-0002-4490-3370

Mackenzie Gutierrez

Department of Physiology and Pharmacology, University of Calgary, Calgary, AB, Canada.

William Nguyen

University of Calgary

Ellen Ren

University of Calgary

Chunlong Mu

University of Calgary https://orcid.org/0000-0001-9405-5907

Erik van Tilburg Bernardes

University of Copenhagen https://orcid.org/0000-0001-5005-2835

Thaís Glatthardt

University of Calgary https://orcid.org/0009-0007-1653-2166

Blanca Callejas

University of Calgary

Simon Hirota

University of Calgary

Jane Shearer

University of Calgary

Article

Keywords: Candida albicans, gut mycobiome, host energy metabolism, interkingdom interactions, bile acids, adipose tissue immunity

Posted Date: September 15th, 2026

DOI: https://doi.org/10.21203/rs.3.rs-10996465/v1

License: This work is licensed under a Creative Commons Attribution 4.0 International License.
Read Full License

Additional Declarations: There is **NO** Competing Interest.

Gut Commensal *Candida albicans* Constrains Whole-Body Energy Storage in Mice

Mackenzie W. Gutierrez[1,2,3,4], William Nguyen[1,2,3,4], Ellen Ren[1,2,3,4], Chunlong Mu[5], Erik van Tilburg Bernardes[1,2,3,4,6], Thaís Glatthardt[1,2,3,4], Blanca E. Callejas[2,4], Simon A. Hirota[2,4], Jane Shearer[5], Marie-Claire Arrieta[1,2,3,4]

[1]Department of Pediatrics, University of Calgary, Calgary, Canada.
[2]Department of Physiology and Pharmacology, University of Calgary, Calgary, Canada.
[3]International Microbiome Centre, Snyder Institute, University of Calgary, Calgary, Canada.
[4]Snyder Institute for Chronic Diseases, University of Calgary, Calgary, Canada.
[5]Department of Biochemistry and Molecular Biology, University of Calgary, Calgary, Canada.
[6]LEO Foundation Skin Immunology Research Center, Department of Immunology and Microbiology, University of Copenhagen, Copenhagen, Denmark.

*Corresponding author. Email: marie.arrieta@ucalgary.ca

Abstract

Candida albicans is a prevalent member of the gut microbiome and a potent modulator of host immunity, yet its role in metabolic regulation remains unclear. Using gnotobiotic mice colonized with a defined bacterial community (Oligo-MM12) with or without *C. albicans*, we demonstrate that persistent, non-infectious colonization with this yeast constrains host energy storage and confers resistance to diet-induced obesity. *C. albicans* colonization remodeled the bacterial

microbiome and bile acid landscape, selectively depleting conjugated bile acids and reducing lipid uptake in jejunal organoids. In parallel, *C. albicans* colonization enhanced adipose mitochondrial respiration and thermogenic programming while promoting a Type 17 immune response, revealing coordinated metabolic and immune adaptations. Genetic deficiency of γδ T cells partially reversed the metabolic phenotype, demonstrating that this immune function contributes to fungal regulation of host energy balance. Together, our findings demonstrate that coordinated interactions among the microbiota, microbial metabolites and the immune system constrain host energy storage by simultaneously limiting nutrient acquisition and enhancing energy expenditure. More broadly, these findings establish intestinal fungi as potent regulators of host metabolism and reveal that low-abundance members of the microbiome can exert disproportionate physiological effects through interkingdom ecological interactions.

Keywords: *Candida albicans*, gut mycobiome, host energy metabolism, interkingdom interactions, bile acids, adipose tissue immunity

Main

The gut microbiota regulates host energy balance through various mechanisms, including coordinated effects on nutrient absorption, bile acid metabolism, adipose tissue thermogenesis and immune function[1-5]. While bacterial contributions to these processes have been extensively characterized, whether intestinal fungi contribute directly to host energy homeostasis remains largely unknown. Given the central role of fungi in mediating nutrient exchange and energy metabolism across diverse symbiotic relationships, from plant–mycorrhizal associations to insect–fungal mutualisms[6-8], persistent fungal colonization may similarly influence energy

balance in mammalian hosts.

Among intestinal fungi, *Candida albicans* is one of the most prevalent commensal species in humans[9-13]. Although best known as an opportunistic pathogen capable of causing mucosal and systemic infections, *C. albicans* also contributes to host physiology during asymptomatic colonization by promoting immune maturation and enhancing protection against subsequent fungal infection[9,14,15]. Emerging evidence suggests that these host interactions may extend beyond immune regulation to include metabolic homeostasis[16-18]. We previously demonstrated that early-life colonization with *C. albicans* in gnotobiotic mice confers resistance to diet-induced obesity (DIO) and is accompanied by marked remodeling of white adipose tissue (WAT) immunity. However, how intestinal fungal colonization is translated into systemic metabolic regulation remains unknown.

Here, we investigated the mechanisms by which early-life intestinal colonization with *C. albicans* regulates host energy balance. Using gnotobiotic mice in combination with intestinal organoids, high-resolution respirometry, immunophenotyping and functional genetic approaches, we examined how fungal colonization influences intestinal nutrient handling, adipose tissue metabolism and immune function to define the pathways linking a common fungal symbiont to whole-body energy homeostasis.

Results

Early-life C. albicans colonization confers resistance to diet-induced obesity

To investigate how early-life fungal colonization influences host energy metabolism, we used our previously established gnotobiotic DIO model[17], in which mice were colonized from

66 birth with either Oligo-MM12 alone (B-only) or in combination with *C. albicans* (B+C), and
67 were weaned onto standard (SD) or a high-fat, high-sucrose (HFHS) diets until 14 weeks of age
68 (**Figure 1A**). Fungal ITS rDNA was detected in the feces of B+C mice at 14 weeks of age, with a
69 reduction in fungal load on HFHS (**Figure 1B-C**), indicating persistent intestinal colonization
70 into adulthood. Consistent with our previous findings[17], *C. albicans* colonization had a
71 significant effect on bacterial beta-diversity and relative abundance (**Figure 1D-E**), highlighting
72 interkingdom interactions between gut bacteria and this common yeast. Across both dietary
73 conditions, *Bifidobacterium animalis* subsp. *animalis* (strain YL2) was markedly enriched in *C.*
74 *albicans*-colonized mice. Diet-specific changes included enrichment of *Enterococcus faecalis*
75 and *Clostridium innocuum* (I46) and depletion of *Blautia coccoides* (YL58) and
76 *Limosilactobacillus reuteri* (I49) under standard diet, whereas HFHS-fed mice exhibited reduced
77 *Enterococcus faecalis* (KB1) and increased *Enterocloster clostridioforme* (YL32) following *C.*
78 *albicans* colonization (**Figure 1E**).

79 Mice colonized with *C. albicans* on either diet displayed a reduction in body weight,
80 percentage of body fat mass and gonadal WAT (gWAT) fat pad weights, and a reciprocal increase
81 in lean mass in both males and females (**Figure 1F-I, Figure S1A-D**). These reductions in body
82 weight and fat mass occurred despite unchanged food intake on the HFHS diet, and increased
83 food intake in *C. albicans* colonized mice fed the SD (**Figure S1E-F**). Importantly, this
84 phenotype was not explained by disseminated colonization or infection, as *C. albicans* was only
85 found in feces and not recovered from blood, skin, liver or kidney tissue (**Figure S1G**). Together,
86 these findings indicate that the metabolic effects of *C. albicans* arise from persistent, non-
87 infectious intestinal colonization rather than reduced food intake or systemic dissemination,
88 suggesting altered host energy balance.

C. albicans reshapes the bile acid landscape and reduces intestinal lipid absorption

To begin defining the mechanisms underlying this metabolic phenotype, we first asked whether *C. albicans* colonization alters intestinal lipid absorption by reshaping the luminal environment that regulates fatty acid uptake. Using an inverted jejunal enteroid system, in which the apical epithelial surface is directly accessible to the culture media[19], we observed that exposure to sterile fecal extracts from B-only mice enhanced oleic acid uptake, consistent with previous studies demonstrating that the gut microbiota promotes intestinal nutrient absorption and metabolic adaptation to dietary lipids[20] (**Figure 2A–B**). This effect was further potentiated by IL-17, consistent with the pro-absorptive metabolic effects of intestinal IL-17 signaling observed *in vivo*[21,22], validating the responsiveness of the enteroid system to host-derived signaling (**Figure S2A-B**). Consistent with known regional differences in intestinal lipid absorption, lipid uptake was greatest in jejunal enteroids[23] (**Figure S2C**). In contrast, sterile fecal extracts from B+C mice markedly suppressed oleic acid uptake, an effect that persisted even in the presence of IL-17 (**Figure 2A–B**), indicating the emergence of a dominant inhibitory signal capable of overriding host-derived pro-absorptive cues.

Given the central role of bile acids in lipid emulsification and absorption, we next examined whether fungal colonization altered the bile acid landscape. Principal component analysis (PCA) revealed a significant shift in overall bile acid composition in B+C mice relative to B-only (PERMANOVA $R^2 = 0.151$, $p = 0.032$; **Figure 2C**). This shift was not global across all bile acids but instead reflected selective remodeling of specific species and functional pools. Notably, *C. albicans* colonization increased alpha-muricholic acid (alpha-MCA) and deoxycholic acid (DCA), while reducing the abundance of conjugated secondary bile acids and

112 total secondary bile acids (**Figure 2D-H, Table S1-S2**). Conversely, unconjugated secondary
113 bile acids were increased (**Figure 2G, Table S2)**, indicating a redistribution toward a bile acid
114 pool predicted to be less efficient at supporting micelle formation and dietary lipid absorption[24].

115 To determine whether bile acids mediated the observed effects on lipid uptake, we
116 repeated the enteroid assay in the presence of cholestyramine, a bile acid sequestrant resin[25]. In
117 extracts from B-only mice, bile acid depletion significantly reduced oleic acid uptake in jejunal
118 enteroids, demonstrating that microbiome-derived bile acids are required to support epithelial
119 lipid absorption (**Figure 2I-J**). In contrast, cholestyramine had no additional effect on extracts
120 from B+C mice, indicating that the bile acid pool in these animals is already functionally
121 impaired. Notably, these effects were not observed in ileal enteroids, consistent with regional
122 differences in intestinal lipid absorption (**Figure S2D**).

123 Given the marked changes in bile acid composition, we next examined whether fungal
124 colonization altered farnesoid X receptor (FXR) signaling. Although sterile fecal extracts
125 robustly activated FXR in a bile acid-dependent manner, as evidenced by loss of reporter activity
126 following cholestyramine treatment, FXR activation was comparable between B-only and B+C
127 mice (**Figure S2E**). Thus, despite substantial remodeling of the bile acid pool and impaired bile
128 acid-dependent lipid uptake, fungal colonization did not measurably alter FXR activation.
129 Collectively, these data support a model in which *C. albicans* reshapes microbiome-derived bile
130 acid metabolism, selectively depleting conjugated secondary bile acids, thereby impairing
131 epithelial lipid uptake.

132

133 *C. albicans promotes thermogenic programming and mitochondrial respiration in WAT*

134 Because adipose tissue regulates whole-body energy expenditure through coordinated

thermogenic and mitochondrial programs, we next examined whether *C. albicans* colonization impacts these processes across white and brown adipose depots, providing a potential mechanism for the reduced adiposity observed in *C. albicans* colonized mice (**Figures 1H-I** and **S1A-B**). We first evaluated the expression of thermogenesis-associated genes in various adipose tissue depots. Because adipose tissue thermogenic responses are known to differ between sexes[26], analyses were stratified by sex. In gWAT, *C. albicans* colonization increased *Ucp1* expression in HFHS-fed males and SD-fed females, *Pgc1α* expression in both sexes on HFHS diet, and *Prdm16* expression in HFHS-fed males. In contrast, *Cd137* expression was reduced in HFHS-fed B+C females (**Figure 3A-B**). In subcutaneous white adipose tissue (scWAT), *C. albicans* colonization similarly induced a thermogenic transcriptional program, increasing the expression of *Ucp1*, *Pgc1α* and *Tbx1* in males on both diets (**Figure S3A-B**). In females, *Tbx1* expression was increased in B+C on HFHS, whereas *Cd137* was elevated on both diets and *Prdm16* was reduced on HFHS. In brown adipose tissue (BAT), *C. albicans* increased *Ucp1* expression in HFHS-fed males, whereas females exhibited reduced *Ucp1* expression accompanied by a trend toward increased *Pgc1α* expression ($p = 0.053$; **Figure S3C-D**). Together, these findings indicated that *C. albicans* colonization promotes depot- and sex-specific transcriptional remodelling consistent with enhanced thermogenic capacity and mitochondrial biogenesis.

To determine whether the thermogenic transcriptional program induced by *C. albicans* was accompanied by enhanced mitochondrial remodeling, we next assessed mitochondrial abundance and function in gWAT, given the determinant role of visceral adipose tissue in systemic metabolic homeostasis[27]. Mitochondrial abundance was quantified using two complementary approaches: mitochondrial DNA copy number and quantitative fluorescence

158 microscopy. Microscopy revealed increased mitochondrial volume in females under both dietary
159 conditions, whereas no differences were observed in males (**Figure 3C–D, E, G**). Consistent
160 with these findings, mitochondrial DNA copy number was increased in *C. albicans*-colonized
161 females fed the SD and showed a similar trend under the HFHS diet (p=0.067), while remaining
162 unchanged in males (**Figure S3E-F**). Interestingly, despite the absence of increased
163 mitochondrial volume or DNA copy number, male mice exhibited a marked reduction in
164 adipocyte volume under both diets, whereas females displayed reduced adipocyte size only under
165 the HFHS diet (**Figure 3F, H**).

166 We next determined whether these transcriptional and structural changes were
167 accompanied by enhanced mitochondrial oxidative function using high-resolution respirometry
168 (**Figure S3G**). This technique quantifies features of mitochondrial oxidative metabolism, such as
169 respiratory capacity of individual electron transport system (ETS) complexes, providing insight
170 into overall respiratory control and respiratory response to specific substrates[28]. In both sexes, *C.*
171 *albicans* colonization increased complex I leak respiration (CI_L) under both diets, and enhanced
172 complex I linked respiration (CI_P), complex I+II linked respiration ($CI+II_P$) and max ETS
173 respiration in SD-fed mice (**Figure 3I-P**). ATP production was also increased in SD-fed females,
174 (**Figure 3Q-R**). In summary, *C. albicans* colonization increased several respiration states in
175 WAT, although the magnitude of oxygen flux is substantially greater in females. Together, these
176 findings indicate that *C. albicans* enhances adipose oxidative metabolism through coordinated
177 transcriptional, structural and functional remodeling of thermogenic pathways, although the
178 underlying adaptations differ across adipose depots and sexes.

179

180 *C. albicans remodels the WAT immune landscape through a type 17 immune response*

Immune cell networks within WAT help regulate not only tissue inflammation but also its endocrine and thermogenic functions[29]. Having established that *C. albicans* enhances thermogenic programming and mitochondrial respiration in WAT, we next asked whether immune remodeling contributes to these mechanisms. We previously showed that intestinal *C. albicans* colonization induces a Type 1/17 inflammatory environment in WAT, characterized by expansion of multiple lymphoid and myeloid populations[17]. However, whether these immune changes regulate the enhanced thermogenic capacity observed in colonized mice remained unknown. We therefore profiled immune cell populations with established roles in adipose thermogenic regulation, including γδ T cells[30], eosinophils[31], natural killer T (NKT) cells[32] and type 2 innate lymphoid cells (ILC2s)[33] (**Figure 4A–D, Table S3-6**).

Among immune populations with established thermogenic functions, eosinophils were reduced in male and female B+C mice, whereas NKT cells increased in HFHS-fed female and male mice. Most notably, γδ T cells were consistently expanded across both sexes and diets, including populations producing IL-17A and TNF-α **(Figure 4A-D)**, cytokines previously shown to induce thermogenic programs in adipocytes[30]. In addition, the proportion of $CD27^+$ γδT cells was reduced, consistent with increased activation of this T cell subset (**Table S3-6**), making γδ T cells compelling candidates to mediate the enhanced thermogenic phenotype. Furthermore, *C. albicans* colonization also increased IL-17A-producing $CD4^+$ T cells and IL-$17A^+$ innate lymphoid cells (ILCs) (**Figure 4A–D**). Although these populations have not been shown to directly drive adaptive thermogenesis, their expansion indicates that multiple immune cell types contribute to the elevated IL-17A environment within WAT, a cytokine previously implicated in the regulation of adaptive thermogenesis[30]. Together, these findings suggest that the phenotype induced by *C. albicans* involves coordinated remodeling of the WAT immune landscape,

encompassing activated γδ T cells, NKT cells and additional IL-17A-producing lymphoid populations.

To determine if γδT cells are required for the lean phenotype induced by *C. albicans*, γδT cell deficient mice, which lack γδTCR expression but retain normal αβ T cell development[34], were rederived germ-free, colonized as B or B+C mice, and subjected to the same DIO protocol as wild-type animals. Loss of γδ T cells partially rescued the metabolic phenotype induced by *C. albicans*. Male B+C mice became less resistant to DIO, exhibiting increased weight gain on the HFHS diet, with only a trend toward reduced body weight relative to B-only controls (Male HFHS AUC, p=0.066; **Figure 4E, G**). In females, body adiposity was similarly restored under the SD, although protection against HFHS-induced adiposity remained (**Figure 4F, H**). Despite this partial rescue, γδ T-cell deficiency did not completely abolish the phenotype. *Candida*-colonized mice of both sexes remained significantly leaner than bacteria-only controls and failed to gain weight or adiposity to the same extent as B-only mice (**Figure 4E–H**), indicating that γδ T cells contribute to, but are not solely responsible for the metabolic effects of *C. albicans*. Energy intake was reduced in *C. albicans*-colonized γδTCR-deficient mice on both diets at 8 weeks of age (**Figure S4A–B**), which may have contributed to the remaining phenotype or simply reflected their smaller body size.

Given that γδT cells play an important role in mucosal anti-fungal defense[35], we also evaluated whether this residual phenotype could be explained by impaired control of *C. albicans* or bacterial growth in the gut, resulting in dissemination and infection. Fecal fungal burden was comparable between γδT cell-deficient and wild-type mice (**Figure S4C**), and neither fungal nor bacterial dissemination was detected in blood, liver and kidneys (**Figure S4D-E**), indicating that the observed metabolic phenotype was not attributable to microbial dissemination.

Finally, to determine whether γδT cells from *C. albicans*-colonized mice were sufficient to promote adipocyte thermogenesis, we differentiated primary adipocytes from the stromal vascular fraction (SVF) of B-only mice and co-cultured them with sex matched γδT cells isolated from WAT. Adipocytes co-cultured with γδ T cells from *C. albicans*-colonized mice did not exhibit increased expression of *Ucp1* or *Pgc1a* compared with adipocytes cultured with γδ T cells from bacteria-only mice (**Figure S5**). Likewise, co-culture with the corresponding non-γδ T-cell fraction failed to induce thermogenic gene expression irrespective of colonization status. These findings indicate that neither γδ T cells nor other WAT immune cell populations are sufficient to recapitulate the thermogenic program induced by *C. albicans*, supporting the requirement for additional signals within the remodeled adipose tissue microenvironment.

Discussion

In this study, we identify the common intestinal commensal *C. albicans* as a previously unrecognized regulator of host metabolic adaptation. We demonstrate that persistent, non-infectious intestinal fungal colonization confers resistance to DIO through coordinated effects on nutrient acquisition and adipose tissue metabolism. Mechanistically, *C. albicans* remodels the bacterial microbiome and bile acid landscape to reduce bile acid-dependent intestinal lipid uptake while simultaneously promoting thermogenesis and mitochondrial remodeling of WAT accompanied by profound immune changes. Together, these findings expand the current paradigm of microbiome-mediated metabolic regulation beyond bacteria, establishing persistent intestinal fungi as integral components of the microbial networks governing host metabolic homeostasis.

Unlike previously reported microbiota-mediated obesity-resistant phenotypes, which are

associated with enhanced thermogenesis and improved or preserved metabolic health[36-38], *C. albicans* colonization induced a distinct physiological state characterized by constrained energy storage. Despite preserved, and in some settings increased, food intake, *C. albicans*-colonized mice remained resistant to DIO while exhibiting coordinated adaptations that simultaneously reduced energy acquisition and enhanced energy dissipation. Specifically, this phenotype combined reduced bile acid-dependent intestinal lipid uptake with impaired adipose expansion during prolonged obesogenic feeding while increasing mitochondrial oxidative capacity and reshaping adipose immune function. The capacity of adipose tissue to expand safely during caloric excess is a hallmark of metabolic health, whereas impaired adipose plasticity may limit energy storage despite nutrient availability[39-41]. Thus, our findings suggest that *C. albicans* colonization may not promote a homeostatic lean phenotype, but rather induces a coordinated physiological state characterized by constrained energy storage. This state may represent an immunometabolic trade-off, analogous to that recently described for asymptomatic intestinal *C. albicans* colonization, which enhances protection against invasive fungal infection while increasing susceptibility to allergic disease[14]. We propose that maintaining a stable non-infectious relationship with a persistent fungal pathobiont carries inherent energetic costs, requiring continuous immune surveillance that ultimately constrains host energy storage.

Mechanistically, our findings suggest that the metabolic effects of *C. albicans* arise from the integration of several partially independent processes rather than from a single dominant mechanism. Previous studies have demonstrated that the gut microbiota coordinates nutrient acquisition with peripheral metabolic adaptation by simultaneously regulating intestinal absorption, adipose remodeling and endocrine signaling in response to environmental and dietary cues[5,20,36]. Our study extends this systems-level framework to a persistent fungal symbiont,

showing that coordinated changes in intestinal nutrient handling, adipose oxidative function and immune regulation converge on a metabolic phenotype. The partial rescue observed in γδ T cell-deficient mice and the absence of differential FXR activation further indicate that neither immune activation nor bile acid receptor signaling alone is sufficient to explain the metabolic changes observed. Instead, our findings support a model in which *C. albicans* reshapes host energy balance through the cumulative actions of microbial, epithelial, immune and adipose tissue networks.

The altered bile acid landscape further suggests that *C. albicans* regulates host nutrient acquisition indirectly through interkingdom interactions within the gut ecosystem. Our previous work demonstrated that individual intestinal fungi, including *C. albicans*, generate species-specific host metabolic phenotypes by restructuring bacterial community composition and metabolic output[17]. The present findings broaden this concept by identifying bile acid metabolism as one functional consequence of these ecological interactions. Because the canonical pathways responsible for bile acid deconjugation and secondary bile acid formation are bacterial[42], the observed remodeling of the bile acid pool is most plausibly explained by fungal-driven changes in bacterial community function rather than direct fungal metabolism. Consistent with this interpretation, *C. albicans* selectively remodeled bacterial taxa with established roles in bile acid homeostasis, including expansion of *B. animalis* and reductions in *B. coccoides* and *L. reuteri*, all of which have independently been implicated in regulating bile acid composition through complementary mechanisms[43-45]. Together with recent studies demonstrating that microbiota-dependent remodeling of bile acid composition regulates intestinal lipid absorption[1,20], our findings support a model in which *C. albicans* indirectly impairs nutrient uptake by reshaping the functional metabolic output of the bacterial microbiome.

While these findings identify impaired nutrient acquisition as one arm of the metabolic phenotype, host energy balance is equally determined by energy expenditure. Our findings identify adipose mitochondrial remodeling as a major component of the host metabolic response to persistent *C. albicans* colonization. Rather than being confined to classical BAT, adaptive thermogenesis is now recognized as a highly plastic process involving coordinated mitochondrial increased capacity across multiple white and brown adipose depots[46]. Consistent with this, *C. albicans* induced depot-specific thermogenic transcriptional programs accompanied by increased mitochondrial oxidative capacity in visceral adipose tissue. Interestingly, enhanced respiration was not uniformly associated with increased mitochondrial abundance, suggesting that improved mitochondrial function, rather than mitochondrial biogenesis alone, contributes to the increased oxidative phenotype. Together with the reduced adipocyte size observed in *C. albicans* colonized mice, these findings suggest that persistent fungal colonization promotes functional remodeling of adipose tissue that favors energy dissipation over long-term lipid storage, providing a plausible mechanism for the constrained adipose expansion observed during chronic caloric excess.

A defining feature of host immunity to *C. albicans* is the robust induction of type 17 immune responses, which are essential for maintaining fungal commensalism and controlling mucosal invasion[15,35,47,48]. Our findings suggest that this evolutionarily conserved antifungal program may also contribute to systemic metabolic adaptation. Consistent with previous reports demonstrating that IL-17-producing γδ T cells promote adaptive thermogenesis through stromal IL-33 signaling[30], *C. albicans* colonization expanded activated IL-17A$^+$TNF-α$^+$ γδ T cells within WAT. However, the accompanying increases in IL-17A-producing CD4$^+$ T cells, IL-17A$^+$ ILCs and NKT cells indicate that fungal colonization promotes coordinated type 17 immune

remodeling within adipose tissue rather than selective expansion of a single thermogenic population. Importantly, neither γδ T-cell deficiency nor *ex vivo* γδ T cell-adipocyte co-cultures fully recapitulated or abolished the metabolic phenotype, arguing against a linear model in which one immune population is solely responsible for fungal-induced thermogenesis. Instead, our findings support a model in which persistent *C. albicans* colonization promotes coordinated remodeling of adipose immune networks that collectively contribute to metabolic adaptation.

The complexity of this immune-metabolic landscape became even more apparent when considered alongside the marked sexual dimorphism observed throughout the metabolic phenotype. Although persistent *C. albicans* colonization conferred resistance to DIO in both sexes, the underlying physiological adaptations differed substantially. Females exhibited greater mitochondrial biogenesis and oxidative capacity within visceral adipose tissue, whereas males displayed more pronounced thermogenic transcriptional responses in subcutaneous adipose tissue together with reductions in adipocyte size despite unchanged mitochondrial abundance. Likewise, adipose immune remodeling was sexually dimorphic, including differences in thermogenic gene expression, immune cell composition and the relative contribution of γδ T cells to the overall phenotype. These findings suggest that biological sex influences how microbial signals are integrated within metabolic tissues. This is consistent with the growing recognition that adipose tissue plasticity and immune-metabolic crosstalk are fundamentally influenced by biological sex[40,49], and with evidence that host sex shapes the physiological consequences of microbiome-host interactions[50]. Together, our findings highlight biological sex as a key determinant of fungal-mediated metabolic adaptation and reinforce the importance of incorporating both sexes into mechanistic studies of microbiome regulation of host metabolism.

Collectively, these mechanistic observations argue against a single dominant pathway

underlying fungal regulation of host metabolism. Instead, our findings support an ecological model in which the physiological consequences of *C. albicans* colonization emerge from the integration of microbial ecology and host responses. Our data suggest that *C. albicans* indirectly influences nutrient acquisition by reshaping bacterial community composition and bile acid landscape, while simultaneously eliciting the canonical Type 17 immune response that promotes adipose immunometabolic remodeling. It is the combination of these pathways, and potentially other unmeasured processes, that fully explain the observed phenotype. Together, they provide a framework in which ecological and host-derived processes converge to constrain host energy storage. This ecological model also has broader implications for our understanding of microbiome-mediated host physiology. The intestinal microbiome has emerged as a central regulator of host energy balance, yet this paradigm has largely been built around a bacteria-centric view. Comprising less than 1-2 % of the intestinal microbial biomass in humans and only 0.1% in mice[9,51], fungi have traditionally been regarded as minor community members with limited physiological relevance. Our findings challenge this view by demonstrating that persistent colonization with a single commensal fungal species can exert profound effects on host energy balance. More broadly, these findings suggest that ecological influence, rather than numerical abundance, may better predict the physiological importance of individual microbial kingdoms. This perspective supports moving beyond kingdom-centric models of microbiome function toward an integrated ecological framework in which host metabolic physiology emerges from interactions among multiple microbial kingdoms and the host.

Our study is limited by the use of a gnotobiotic mouse model containing a simplified bacterial community, which enabled mechanistic dissection of fungal–host interactions while reducing the ecological complexity of the conventional gut microbiome. Whether the

mechanisms identified here are conserved in more diverse microbial ecosystems remains to be established. Nevertheless, long-term intestinal *C. albicans* colonization similarly reduced weight gain and remodeled bacterial communities in conventionally colonized mice[52], suggesting that the physiological effects of fungal colonization are not unique to simplified microbial ecosystems. Although our findings support an integrated model linking fungal-induced bacterial remodeling, bile acid metabolism and nutrient absorption, the relative contributions of individual taxa, microbial functions and bile acid transformations remain unresolved. Likewise, the gut-derived signals that communicate intestinal fungal colonization to adipose tissue and drive mitochondrial, thermogenic and immune remodeling have yet to be identified. Finally, establishing the translational relevance of these findings will require defining the ecological conditions that permit fungal regulation of host metabolism in humans. More broadly, our findings suggest that routine integration of mycobiome profiling into microbiome studies of metabolic health may uncover previously unrecognized ecological drivers of metabolic states and adaptations.

Methods

Gnotobiotic mice

Adult germ-free (GF) C57Bl/6J mice were obtained from in-house breeding colonies in the International Microbiome Centre (IMC) at the University of Calgary. Specific pathogen free B6-TCRdelta- mice (B6.129P2-Tcrd^{tm1Mom}/J; Strain #002120) were purchased from the Jackson Laboratory and rederived GF through the axenic embryo transfer program in the IMC. Six to twelve-week-old wild-type or B6-TCRdelta- C57BL/6J female mice were orally gavaged twice, 2 days apart, with 100 µL of a consortium of organisms. These consortia included (i) the Oligo-

MM12[53] alone "B" (*Acutalibacter muris KB18, Akkermansia muciniphila YL44, Bacteroides caecimuris I48, B. animalis YL2, B. pseudococcoides YL58, C. innocuum I46, E. clostridioformis YL32, E. faecalis KB1, Flavonifractor plautii YL31, L. reuteri I49, Muribaculum intestinale YL27,* and *Turicimonas muris YL45)* or in combination with (ii) *C. albicans* (isolated from human infants enrolled in the ANTIBIO Study, Alberta Children's Hospital[13]) "B+C". Each colonization group was kept in a separate gnotobiotic isolator. Inoculum were prepared under anaerobic conditions by combining 100 µL of 3-day-old cultures of each bacterial strain and a 1-day-old culture of *C. albicans*. Bacteria were grown in fastidious anaerobe broth (Lab M Limited, United Kingdom) at 37°C, *C. albicans* was grown in yeast-mold (YM) broth (Becton Dickson, USA) at room temperature (RT). After the initial gavage, females were paired with males (six to ten weeks old) for mating at a 2:1 ratio, respectively. To support early-life exposure, *C. albicans* culture was spread on the dams' abdomen and nipple regions twice on days 2-6 after birth, as previously described[54]. Mice were kept at maximum of five animals per cage, under a 12-hour light/dark cycle, 40% relative humidity, 22-25°C and *ad libitum* access to sterile food and water. All experiments were conducted under protocols approved by the University of Calgary Animal Care Committee, following the guidelines of the Canadian Council on Animal Care (AC20-0176).

DIO model

At 21-days of age, mice were weaned onto powdered SD (LabDiet JL Rat and Mouse/Auto 6F 5K52; LabDiet, USA) or HFHS (DYET#1013915 for 3-12 weeks of age and DYET#102412 after 12 weeks of age; Dyets, Inc., USA) and remained on the diets until the experimental endpoint. To ensure sterility, the HFHS diet was irradiated (5-20 kGy) and both

diets were autoclaved at 132°C for 30 minutes. Body weight was measured weekly and following export from gnotobiotic isolators, whole-body fat and lean mass was measured by TD-NMR with the Minispec LF90II (Bruker, USA). gWAT weight was determined at the endpoint.

Quantification of viable fungal load

Fungal load was assessed by culturing feces, blood, kidney or liver collected at 10 weeks of age on selective media. Mouse fecal pellets were weighed and homogenized in 500 µL of sterile PBS (Corning, USA) at 15 Hz for 2 min. Homogenates were serially diluted in sterile PBS. Tissues were homogenized in 1mL of sterile PBS with a steel bead at 30 Hz, for 3 min. Samples were spread on YM agar plates supplemented with gentamycin (10 µg/mL; Sigma-Aldrich, USA) and chloramphenicol (200 µg/mL; Sigma-Aldrich, USA). Plates were incubated at RT for 3 days before colonies were counted to determine viable fungal concentration.

Genomic DNA isolation

Genomic DNA was extracted from mouse fecal pellets collected at the indicated time points using the DNeasy PowerSoil Pro Kit (Qiagen, Germany) according to the manufacturer's protocol. To improve microbial cell lysis, samples were subjected to mechanical disruption using a TissueLyser II bead beater (Qiagen, Germany) prior to DNA purification. Purified DNA was eluted in nuclease-free water and stored at −20°C until analysis by quantitative PCR (qPCR) or 16S rRNA gene amplicon sequencing.

Quantification of fungal DNA by qPCR

Fungal abundance in fecal samples collected at 12 weeks of age was quantified by real-time PCR targeting the internal transcribed spacer (ITS) region[55]. Reactions were performed on a StepOne Plus Real-Time PCR System (Applied Biosystems, USA) in a final volume of 20 µL containing 10 µL iQ SYBR Green Supermix (Bio-Rad Laboratories, USA), 100 nM ITS1F (5′-CTTGGTCATTTAGAGGAAGTAA-3′), 500 nM ITS4 (5′-TCCTCCGCTTATTGATATGC-3′), 1 ng template DNA, and nuclease-free water. Amplification conditions consisted of an initial denaturation at 95°C for 5 min, followed by 32 cycles of 95°C for 30 s, 55°C for 30 s, and 72°C for 1 min. A melt curve analysis (95°C for 15 s, 60°C for 1 min, 95°C for 15 s, and 60°C for 15 s) was performed to confirm amplification specificity. All samples were analyzed in duplicate, and fungal DNA concentrations were determined by comparison with a standard curve generated from serial dilutions of *C. albicans* genomic DNA.

Adipose thermogenesis and mitochondrial genes expression by RT-qPCR

Tissues were stored in RNA later (Thermo Fisher, USA) at 4°C overnight before being stored at -80°C. RNA was isolated using the RNeasy Lipid Tissue Mini Kit (Qiagen, Germany) according to the manufacturer's instructions. Reverse transcription was performed with the All-in-One 5X RT MasterMix (Applied Biological Materials Inc., Canada). cDNA quality was assessed using the NanoDrop spectrophotometer (Thermo Fisher, USA) and samples were topped up to 50 µL per µg of RNA that was reverse transcribed. PCR reactions were performed with iQ SYBR Green Supermix (BioRad, USA) on the QuantStudio 3 Real-Time PCR System (Applied Biosystems, USA). 20 µL reactions were run in triplicate with the following cycling protocol: initial 2 min step at 94°C, followed by 40 cycles of 94°C for 15 s and 50°C for 1 min, and a final melt curve of 95°C for 15 s, 60°C for 1 min, 95°C for 15 s and 60°C for 15 s.

Primers were selected from previous publications[30,31,56] and are as follows: *18S* (forward, 5'-CACGGCCGGTACAGTGAAAC-3'; reverse 5'-AGAGGAGCGAGCGACCAA-3'), *Ucp1* (forward, 5'-GGCCTCTACGACTCAGTCCA-3'; reverse 5'-TAAGCCGGCTGAGATCTTGT-3'), *Tbx1* (forward, 5'-CGCACAGTGGATGAAACAGA-3'; reverse 5'-TGTCTTTTCGAGGGTCCACA-3'), *Pgc1α* (forward, 5'-TGAAGACGGATTGCCCTCAT-3'; reverse 5'-TGGTGCCAGTAAGAGCTTCT-3'), *Cd137* (forward, 5'-CGTGCAGAACTCCTGTGATAAC-3'; reverse 5'-GTCCACCTATGCTGGAGAAGG-3'), *Il33* (forward, 5'- ATGGGAAGAAGCTGATGGTG-3'; reverse 5'-CCGAGGACTTTTTGTGAAGG-3'), *Dio2* (forward, 5'-TGCCACCTTCTTGACTTTGC-3'; reverse 5'-GGTTCCGGTGCTTCTTAACC-3'). Fold gene expression was calculated with the $2^{-\Delta\Delta Ct}$ method with *18S* serving as the housekeeping gene.

16S rRNA amplicon sequencing

Genomic DNA was submitted to Microbiome Insights (Vancouver, Canada) for 16S rRNA gene amplicon sequencing. The V4 hypervariable region was amplified using the universal primer pair 515F/806R[57] and Phusion Hot Start II DNA Polymerase (Thermo Scientific, USA). All samples were processed and sequenced within the same sequencing run to avoid batch effects. Amplicons were purified, normalized using the SequalPrep Normalization Plate Kit (Applied Biosystems, USA), and quantified with the KAPA Library Quantification Kit (Roche, Switzerland) prior to pooling into dual-indexed sequencing libraries[58]. Negative PCR controls (no-template reactions) and mock microbial communities containing defined bacterial and fungal compositions were included throughout library preparation and sequencing to monitor

contamination and sequencing performance. Pooled libraries were denatured, diluted, and sequenced using paired-end chemistry on an Illumina MiSeq platform (Illumina Inc., USA).

Amplicon sequence processing

Raw sequence data were processed in R v4.1.1 using the DADA2 v1.20.0 pipeline [59]. Reads were quality filtered, trimmed, denoised, merged, and screened for chimeric sequences following the standard DADA2 workflow (https://benjjneb.github.io/dada2/tutorial.html). Amplicon sequence variants (ASVs) were assigned using a custom reference database containing the 16S rRNA gene sequences of the Oligo-MM12 bacterial strains[60]. ASVs that could not be assigned to one of the Oligo-MM12 members were classified as "Other". Downstream processing was performed using the phyloseq package v1.36.0[61]. A total of 191 ASVs were initially identified. Samples containing fewer than 1,000 sequencing reads were excluded, and ASVs detected in only a single sample were removed. The dataset was subsequently filtered to retain ASVs present at least three times in a minimum of 20% of samples, resulting in a final dataset of 15 ASVs that was used for all downstream analyses.

Intestinal organoid generation and Lipid Uptake Assay

Jejunum and ileum tissues were harvested from C57BL/6 mice and processed to isolate intestinal crypts. Intestines were opened longitudinally, washed with cold DPBS, and minced into small pieces. Tissue fragments were washed with cold DPBS and centrifuged at 300 × g for 30 seconds at room temperature.

Tissue fragments were incubated in crypt isolation buffer containing 43.4 mM sucrose (Sigma-Aldrich, USA), 2 mM EDTA (Thermo Fisher Scientific, USA), and 0.5 mM DTT (Thermo Fisher Scientific, USA) in DPBS (Thermo Fisher Scientific, USA) for 30 min at 4 °C with gentle rocking and pelleted at 300 × g for 5 min. Tissue fragments were resuspended in 10 mL DPBS and pipetted repeatedly, allowed to settle, and the resulting supernatants were collected. This procedure was repeated twice, pooled, and passed through a 100 μm cell strainer.

The filtered crypt suspension was centrifuged at 300 × g for 5 min at 4 °C, and the resulting pellet was resuspended in Matrigel (70%; Corning, USA) and plated in 30μL domes. Following Matrigel solidification, domes were fed with complete mouse organoid medium containing GlutaMAX (2 mM; Gibco/Thermo Fisher Scientific, USA), HEPES (10 mM; Thermo Fisher Scientific, USA), N2 supplement (1×; Thermo Fisher Scientific, USA), B27 supplement (1×; Thermo Fisher Scientific, USA), fetal bovine serum (10%; Sigma-Aldrich, USA), WRN-conditioned medium (50%), recombinant human EGF (50 ng/mL; Thermo Fisher Scientific, USA), N-acetylcysteine (1 mM; Sigma-Aldrich, USA), and penicillin/streptomycin (1× Sigma-Aldrich, USA). Y-27632 10 μM; Tocris Bioscience, UK) was included during the initial plating period and omitted during subsequent medium changes. Culture medium was replaced every 2-3 days, and intestinal organoids were passaged every 5–6 days.

For organoid inversion, ileal and jejunal organoids were collected three days after passaging and incubated in 5 mM EDTA in PBS at 4 °C for 1 h to remove Matrigel. Organoids were then washed twice with washing medium containing DMEM/F-12 (Sigma-Aldrich, USA) supplemented with 15 mM HEPES, 10% FBS, L-glutamine (Sigma-Aldrich, USA), and penicillin/streptomycin (final concentration: 100 U/mL and 100 μg/mL, respectively), and

transferred to ultra-low-attachment plates (# 3473, Corning, USA)) for 48 h at 37 °C to generate apical-out organoids. Organoids were fed with mouse complete media supplemented with 10 μM Y27632. For the IL-17-treated group, organoids were treated with IL-17 (421-ML/CF, R&D Systems, USA) at concentrations ranging from 5 to 50 ng/ml for 24 h.

For experimental treatments, apical-out organoids were washed and re-seeded in complete mouse organoid medium containing 0.4 mM oleic acid (Sigma-Aldrich, USA) and or 10% sterile fecal extracts derived from mice colonized with *Candida albicans* or from non-infected control mice in the presence or absence of cholestyramine (MilliporeSigma, Romania). After 24 h of treatment, organoids were washed twice with DPBS to remove residual stimuli and stained with BODIPY 493/503 (Thermo Fisher Scientific, USA) for 20 min at room temperature. Organoids were subsequently washed three times with DPBS and counterstained with phalloidin (Thermo Fisher Scientific, USA) and DAPI (Thermo Fisher Scientific, USA). Finally, apical-out organoids were mounted on concave glass slides with mounting medium for imaging.

Images were acquired using a Nikon A1R Confocal Microscope (Nikon A1R, 20x/0.31 NA objective) equipped for z-stack acquisition. Sequential optical sections were collected at 1 μm intervals using the z-stack function and processed for three-dimensional reconstruction and image analysis. GFP and DAPI signal volume were quantified using FIJI (ImageJ, version v1.54p)[62]. A gaussian blur was applied, followed by thresholding and segmentation across the entire image stack. Signal volume was quantified using the FIJI 3D ImageJ Suite (v4.1.7)[63]. Volume of GFP signal, quantifying lipid droplets, were divided by volume of DAPI, quantifying nuclei, to normalize and compare enteroids of varying sizes.

FXR reporter assay

Mouse stool samples were combined with sterile PBS at 1:5 ratio and homogenized using a Qiagen Tissuelyser II (Qiagen, Germany) at 15 Hz for 1 min. Supernatant was removed and filter sterilized with a 0.22 μm syringe filter. For treatments involving resin, fecal filtrates were treated with cholestyramine resin for 30 min at 2% w/v, then centrifuged at 18,000 ×g for 5 min; the supernatant was removed afterwards. FXR activity was quantified using the Mouse Farnesoid X Receptor Reporter Assay System (Indigo Bioscience, USA) according to manufacturer's instructions. Treatments containing fecal filtrate were diluted to 5% when applied to the assay system.

Quantification of bile acids

Sample preparation

Fecal samples were thawed on ice then extracted with ice-cold methanol in a 2:1 (v/w) ratio (μL/mg). Samples were homogenized at 30 Hz for 3 min on a homogenizer (Bead Ruptor 96, OMNI international) equipped with microcentrifuge tube tissueLyser adapter sets (2x24, Qiagen, Germany). After centrifugation at 18 000 ×g for 10 min at 4 °C, supernatants were collected and centrifuged again under the same conditions. Clear supernatants were diluted 1:3 with 50% ice-cold methanol (v/v, HPLC-grade) prior to LC-MS/MS analysis.

LC-MS/MS sample analysis

LC-MS/MS analysis was performed on a Vanquish™ ultra high-performance liquid chromatography (UHPLC) system coupled to a TSQ Fortis™ triple quadrupole mass spectrometer (Thermo Fisher Scientific, USA) equipped with an electrospray ionization (HESI-

II) probe. The UHPLC-MS platform was controlled by an Xcalibur™ data system (Thermo Fisher Scientific, USA). Chromatographic separation was achieved on a Accucore ™ C30 column (150 X 2.1 mm, 2.6 µm, Thermo Fisher Scientific, USA) using a binary solvent system composed of LC-MS grade water containing 5 mM ammonium acetate and 0.1% (v/v) formic acid (Solvent A) and LC-MS grade methanol containing 5 mM ammonium acetate and 0.1% (v/v) formic acid (solvent B). The following 55 min gradient, with chromatographic resolution of the monitored isobaric bile acids, was used: 0-2.5 min, 50% B; 2.5-6 min, 50-70% B; 6-10 min, 70% B; 10-34 min, 70-100% B; 34-38 min, 100% B; 38-40 min, 100% B, flow from 100-200 µL min^{-1}; 40-40.5 min, 100-50% B, flow from 200-150 µL min^{-1}; 40.5-44.9 min, 50% B, flow from 150-100 µL min^{-1}; 44.9-55 min, 50% B. Unless otherwise stated, the flow rate was 100 µL min^{-1}. The sample injection volume was 5 µL. The auto sampler was kept at 6°C and the column at 30°C.

MS/MS data were acquired in positive electrospray ionization mode with the mass spectrometer operating in selected reaction monitoring (SRM) mode. Fragmentation parameters were optimized using the EZ Tune program with direct infusion of the analytical grade bile acid standards (50 µM each in 1:1 (v/v) Solvent A/Solvent B). For each bile acid, a pair of quantifier (Quan) and qualifier (Qual) ions was selected. Subsequently, the following transitions were monitored (1-45 min), with a dwell time of 25 ms: Bile acid, $[M+NH4]^+$ *m/z* Parent ion → *m/z* Quan (CE), *m/z* Qual (CE), where CE is the collision energy (V). a-MCA/b-MCA/w-MCA/CA/HCA/UCA, *m/z* 426.3 → *m/z* 355.2 (18), *m/z* 373.2 (13); CDCA/DCA/HDCA/MDCA/UDCA, *m/z* 410.3 → *m/z* 357.2 (11), *m/z* 339.2 (13); GCA, *m/z* 483.3 → *m/z* 412.4 (20), *m/z* 430.4 (17); GCDCA/GDCA/GHDCA/GUDCA, *m/z* 467.4 → *m/z* 414.2 (19), *m/z* 432.2 (13); GLCA, *m/z* 451.3 → *m/z* 416.2 (15), *m/z* 323.2 (26); LCA, *m/z* 394.3

→ *m/z* 359.4 (14), *m/z* 135.4 (35); T-a-MCA/ T-b-MCA/ T-w-MCA/TCA, *m/z* 533.3 → *m/z* 462.2 (20), *m/z* 480.2 (16); TCDCA/TDCA/ THDCA/TUDCA *m/z* 517.3 → *m/z* 464.2 (17), *m/z* 482.2 (13); TLCA, *m/z* 501.3 → *m/z* 466.4 (16), *m/z* 341.3 (24).

Electrospray ionization source conditions were as follows: spray voltage of 3000 V, vaporizer temperature of 325°C, sheath gas of 35 psi, auxiliary gas flow of 10 (arbitrary units) and sweep gas flow of 2 (arbitrary units), capillary temperature of 275°C.

Bile acids in the biological samples were quantified using external standard calibration. A freshly prepared working solution, containing alpha-Muricholic acid (a-MCA), beta-Muricholic acid (b-MCA), omega-Muricholic acid (w-MCA), cholic acid (CA), Ursocholic acid (UCA), Chenodeoxycholic acid (CDCA), Deoxycholic acid (DCA), Hyocholic acid (HCA), hyodeoxycholic acid (HDCA), Murideoxycholic acid (MDCA), ursodeoxycholic acid (UDCA), Glycocholic acid (GCA), Glycochenodeoxycholic acid (GCDCA), Glycodeoxycholic acid (GDCA), Glycohyododeoxycholic acid (GHDCA), Glycoursodeoxycholic acid (GUDCA), Glycolithocholic acid (GLCA), lithocholic acid (LCA), Tauro-alpha-Muricholic acid (T-α-MCA), Tauro-omega-Muricholic acid (T-w-MCA), Taurochenodeoxycholic acid (TCDCA), Taurodeoxycholic acid (TDCA), Taurohyodeoxycholic acid (THDCA), Tauroursodeoxycholic acid (TUDCA), Taurolithocholic acid (TLCA) at 100 µM (final concentration) and HCA, Tauro-beta-Muricholic acid (T-b-MCA), Taurocholic acid (TCA) at 200 µM (final concentration) in MeOH, was further diluted (1:2) in 50% methanol to prepare 15 calibration solutions.

Data analyses were conducted in El-Maven[64] using integrated peak intensity (area under the curve). Reported bile acid concentrations in the samples are corrected for sample dilutions (1:3) prior to LC-MS/MS analysis.

Quantification of mitochondrial density

DNA was isolated from WAT with the RNeasy Lipid Tissue Mini Kit (Qiagen, Germany) according to a manufacturer's protocol. Mitochondrial DNA copy number per cell was then quantified with the Absolute Mouse Mitochondrial DNA Copy Number Quantification qPCR Assay Kit (ScienCell, USA) according to manufacturer's instructions.

Adipose tissue whole-mount fluorescence microscopy

WAT was excised from B and B+C mice and fixed in 4% paraformaldehyde (PFA; Thermo Fisher, UK) overnight at 4°C. Tissue was washed 2x with 0.002% heparin (Sandoz, Canada) in PBS for 30 min, then sandwiched between two microscope slides and secured with clamps for 2 h at 4°C to reduce tissue thickness. Tissue was blocked with 2.5% bovine serum albumin (BSA, MilliporeSigma, USA) + 1% Triton (Thermo Fisher Scientific, USA) in PBS overnight at 4°C. To reduce autofluorescence, tissue was quenched with 0.1% Sudan Black (MilliporeSigma, China) in ethanol for 30 min at RT, then washed with PBS 4x for 1h each time. Mitochondria were stained with TOMM20 directly conjugated to Alexa Fluor 555 (Abcam AB221292; Abcam, USA) at 1:100 in 0.2% Triton in PBS for 2 days at 4°C and washed with PBS 4x for 1h each time. DAPI counterstain (Calbiochem, Germany) was applied at 1:250 for 15 min at RT. Tissue was mounted with a #1.5 coverslip and 200 µm spacer.

Images were acquired using a Nikon A1R Confocal Microscope (Nikon A1R, 60x/1.40 NA Oil objective) equipped for z-stack acquisition. Sequential optical sections were collected at 0.5 µm intervals over a 22.5 µm stack and processed for three-dimensional reconstruction and image analysis. Images underwent thresholding and segmentation across the entire image stack. TOMM20 and adipocyte signal volume were quantified using FIJI ImageJ v1.54p[62] and the FIJI

636 3D ImageJ Suite v4.1.7[63].

637

638 *High-resolution respirometry*

639 At the experimental endpoint, ~20 mg of gWAT was isolated and stored in MiR05 buffer
640 prepared as described previously[65] for up to 1 h. The tissue was minced and macerated before
641 being transferred to a calibrated Oxygraph-2k chamber (Oroboros Instruments, Austria).
642 Digitonin (2 µM) was added to permeabilize the cells and samples were allowed to stabilize for
643 up to 10 min, then titrations were performed based on a previously described protocol with some
644 modifications[66]. Malate (0.5 mM; Sigma, Canada), pyruvate (5 mM; Sigma, Canada) and
645 glutamate (10 mM; Sigma, Canada) were added to measure complex I leak respiration, ADP (5
646 mM; Sigma, Canada) was then added to measure complex I linked respiration. Cytochrome c (10
647 µM; Sigma, Canada) was added to test the integrity of the outer mitochondrial membrane,
648 followed by succinate (10 mM; Sigma, Canada) to measure complex I+II linked respiration.
649 Adenosine triphosphate (ATP) synthase was inhibited with addition of oligomycin (2 µg/mL;
650 Sigma, Canada). Then, trifluoromethoxy carbonylcyanide phenylhydrazone (FCCP; Sigma,
651 Canada) was titrated in steps of 0.5 µM to determine the maximum capacity of the ETS.
652 Rotenone (0.05 µM) was then added to inhibit complex I, followed by Antimycin A (2.5 µM;
653 Sigma, Canada) to inhibit ETS and assess residual oxygen consumption. The total length of the
654 protocol was 90–120 minutes. Total protein concentration of the chamber contents was
655 determined by the Pierce BCA Protein Assay (Thermo Fisher, USA) following manufacturer
656 instructions. Data was analyzed with normalization to protein contents in DatLab v7 (Oroboros
657 Instruments, Austria).

658

Adipose tissue immune cell isolation

gWAT was dissected and placed in DMEM (Gibco, USA) supplemented with 10% inactivated horse serum (iHS; Sigma-Aldrich, USA) and 12.5mM HEPES (Gibco, USA) on ice for up to 1 h. The wet weight of the tissue was obtained, and samples were mechanically minced and placed back in the media. 1 mg/mL of collagenase Type II (Gibco, USA) and 5 KU/mL of DNase I (Sigma-Aldrich, USA) were added to the media and samples were incubated at 37°C with 200 rpm shaking for 25 min and additional manual shaking every 5 min. Samples were supplemented with 0.1M EDTA and incubated at 37°C with 200 rpm shaking for another 5-10 minutes. Once digestion was complete, samples were filtered through 100 μm mesh and topped up with 20 mL DMEM solution. Samples were spun at 300 ×g for 5 min at 4°C. Supernatant was aspirated, and red blood cell lysis was performed with 2 mL ACK Lysing Buffer (Quality Biological, USA) at RT for 3 or 7 minutes for samples from lean or obese mice, respectively. Samples were topped up with 8 mL cold PBS supplemented with 2% iHS (Sigma-Aldrich, USA), filtered through 250 μm mesh, and spun at 300 ×g for 5 min at 4°C. Cells were resuspended in DMEM solution for downstream assays.

In vitro stimulation of adipose tissue immune cells

The bulk SVF from digested gWAT was resuspended in complete RPMI (RPMI supplemented with 10% iHS and 1% penicillin/streptomycin) and stimulated with phorbol 12-myristate 13-acetate (PMA, 50 ng/mL; Sigma-Aldrich) and ionomycin (1 μg/mL; Sigma-Aldrich, USA) for 4 h at 37°C 5% CO_2. Brefeldin A (10 μg/mL; Sigma-Aldrich, USA) was added for the last 3 h. Cells were washed twice in 2% iHS before immunolabelling and flow

cytometry.

Immunolabelling and flow cytometry

Stimulated bulk SVF was stained with LIVE/DEAD Fixable Blue Dead Cell Stain (Invitrogen, USA) and Fcγ-receptor-blocking antibody (Becton Dickson, USA) followed by staining for extracellular markers. Cells were then fixed and permeabilized with the Foxp3/Transcription Factor Staining Buffer Set (eBioscience, USA) and stained for intracellular markers. The following antibodies were from eBioscience: AF532 anti-CD45 (clone 30-F11), PerCP-eF710 anti-RORγt (eBio17B7), AF660 anti-TNFα (MP6-XT22), BUV661 anti-IL-17A (eBio17B7), eF450 anti-IL5 (TRFK5); from BD: BUV395 anti-NK1.1 (PK136), BUV496 anti-CD90.2 (30-H12), BUV563 anti-CD4 (RM4-5), BUV737 anti-CD11b (M1/70), BV650 anti-CD64 (X57-5/7.1), BV711 anti-GATA3 (L50-82), BV750 anti-TCRβ (H57-597), BV786 anti-SigF (E50-2440), PE-CF594 anti-γδTCR (GL3), PE-Cy7 anti-Ly6G (1A8), BUV805 anti-CD3 (17A2); from Biolegend: BUV615 anti-CD11c (N4/18), BV510 anti-MHC-II (M5/114.15.2), BV605 anti-CD27 (LG.3A10). Samples were run on the Cytek Aurora (Cytek Biosciences) and analyzed with FlowJo v10.10.0 (representative gating strategy for cell characterization presented in **Figure S6**).

Primary adipocyte differentiation

C57Bl/6J Oligo-MM12-colonized mice (8-14 weeks of age) were purchased from the IMC. gWAT was dissected, minced and placed in DMEM (Gibco, USA) supplemented with 10% iHS (Sigma-Aldrich, USA), 12.5mM HEPES (Gibco), and 0.2% BSA (Sigma Aldrich, USA) on

ice. 1 mg/mL of collagenase Type I (Gibco, USA) was added to the media and samples were incubated at 200 rpm 37°C for 45 min. Once digestion was complete, samples were filtered through 100 μm mesh and topped up with 20 mL DMEM solution. Samples were spun at 300 ×g for 5 min at 4°C. Supernatant was aspirated, and red blood cell lysis was performed with 2 mL ACK Lysing Buffer (Quality Biological, USA) at RT for 4 min. Samples were topped up with 8 mL cold PBS supplemented with 2% iHS (Sigma-Aldrich, USA), filtered through 40 μm mesh, and spun at 300 ×g for 5 min at 4°C. Cells were plated in 24-well plates at a density of $5x10^4$ cells/well in 1 mL complete high-glucose DMEM (supplemented with 10% FBS and 1% penicillin/streptomycin). Cells were grown to 70-80% confluence (day 0) and treated with insulin (1 μg/mL; Sigma Aldrich, USA), 3-isobutyl-1-methylxantine (0.5 mM, Sigma-Aldrich), dexamethasone (0.25 μM; Sigma-Aldrich, USA) and rosiglitazone (1 μM; TCI America, USA) for 48 h. Cells were then maintained in complete high-glucose DMEM supplemented with insulin (1 μg/ml) until adipocytes were mature (day 8-10) as previously described[67].

γδT cell-adipocyte co-culture assay

SVF was isolated from gWAT as described above, however cells were filtered through 40 μm mesh following red blood cell lysis. Samples underwent dead cell removal and positive selection for γδT cells with MACS MicroBeads (Miltenyi Biotec, USA). γδT cells and the remaining pre-enriched T cell fraction (non-γδT cells) were co-cultured with the primary differentiated adipocytes in complete high-glucose DMEM for 18 h. Isolated cells were plated at an estimate of a biologically representative ratio with differentiated adipocytes based on values reported in the literature and our previous findings. Briefly, the percentage of differentiated

adipocytes was estimated from 3 fields of view across 3 independent wells, and the approximate number of adipocytes was calculated accordingly. We followed literature estimates that the SVF comprises ~70% of the cells in WAT and of those cells ~65% are $CD45^{+}$[68,69]. We used these proportions and the mean proportion of γδT cells (Male: 2.3%, Female: 1.4%) and non-γδT cells ($CD90.2^{+}$ cells without γδT cells; Male: 29.0%, Female: 31.2%) within the $CD45^{+}$ population in B+C mice to determine the ratio of cells to plate relative to number of differentiated adipocytes. Up to 5,000 or 15,000 γδT cells were plated in females and males, respectively. Cells isolated from either sex were co-cultured with primary differentiated adipocytes derived from mice of the same sex. Recombinant mouse IL-17A (1 ng/μL; R&D Systems, USA) was included as a positive control. After 18 hours, the supernatant was removed, and cells were harvested in Qiazol and immediately flash frozen. RNA was isolated and cDNA generated as described above.

Data visualization and statistical analysis

Data were analyzed separately between males and females to assess the sex-related differences in host immune and metabolic responses. The effect of diet and colonization was then analyzed by Two-way ANOVA with Šídák's multiple comparisons test. Differences in trapezoidal area under the curve (AUC) for body weight were assessed by Two-way ANOVA with Šídák's multiple comparisons test. Energy intake was analyzed separately for either diet; normality was assessed by Shapiro-Wilk test and significant differences at each timepoint were defined by unpaired t-test. Adipose tissue qPCR results were analyzed separately between sexes and diets; normality was assessed by Shapiro-Wilk test and significant differences within either diet defined by unpaired t-test or Mann-Whitney U test, accordingly.

For microbiome analysis, beta diversity was calculated using the Bray–Curtis

748 dissimilarity index following variance-stabilizing transformation of the ASV count table and
749 visualized by principal coordinates analysis (PCoA), with ellipses representing the 95%
750 confidence intervals (CI). Differences in community composition between B and B+C mice were
751 assessed using permutational multivariate analysis of variance (PERMANOVA), incorporating
752 sex and diet (12-week time point) as explanatory variables, using the vegan package v2.6-4[70].
753 Differential abundance analysis of the 12 Oligo-MM12 bacterial strains was performed using
754 DESeq2 v.1.38.3[71], comparing each fungal-colonized group with its corresponding B-only
755 control. Resulting p-values were adjusted for multiple comparisons using the Benjamini–
756 Hochberg false discovery rate (FDR) correction. Group comparisons for individual bile acids and
757 grouped bile acids were performed using two-sided Mann–Whitney U tests. To account for
758 multiple comparisons, p-values were adjusted using the Benjamini–Hochberg FDR method.
759 Grouped bile acid metrics were calculated by summing concentrations of predefined bile acid
760 classes for each sample. Statistical testing for grouped metrics followed the same Mann–Whitney
761 U test framework with FDR correction applied across all grouped comparisons. For multivariate
762 analysis, principal component analysis (PCA) was performed on log-transformed bile acid
763 concentrations (log10[x + 1e−6]). Variables were centered and scaled to unit variance prior to
764 PCA. Differences in overall bile acid composition between groups were assessed using
765 PERMANOVA based on Euclidean distances. All statistical analyses were conducted in R.

766 For respirometry, FXR reporter activity, fluorescence microscopy, and enteroid lipid
767 uptake data, the effects of diet and colonization were assessed by two-way ANOVA followed by
768 Šídák's multiple comparisons test. Bar and line plots display the mean with SEM. Immune data
769 was analyzed by unpaired t-test. Flow cytometry data was gated using FlowJo v10.10.0. Graphs
770 were made using GraphPad Prism v10.2.1.

Data availability

The demultiplexed 16S rRNA amplicon sequencing data generated in this study have been deposited in the Sequence Read Archive (SRA) of NCBI under accession code BioProject PRJNA1041856 [https://www.ncbi.nlm.nih.gov/bioproject/?term=PRJNA1041856]. Bile Acid mass spectral raw data will be deposited under study identifier XXX. The metabolic and immune data generated in this study will be provided in the Supplementary Information/Source Data file. All microbial strains are kept as stocks in the Arrieta lab and can be shared when requested.

Code availability

Code will be found at Github

Acknowledgements

We would like to acknowledge Dr. Jennifer Thompson and Taylor Scheidl for support with TD-NMR equipment and primary adipocyte differentiation, as well as the Human Organoids Innovation Hub (HOIH) and the Live cell Imaging (LCI) core at the Snyder Institute for Chronic Diseases, University of Calgary. We would also like to thank Annegret Ulke-Lemee and the staff at the Calgary Metabolomics Research Facility for their support on the bile acid quantification assay.

Author contributions:

Conceptualization: MWG, M-CA

Methodology: MWG, WN, CM, B-CP, SAH, JS, M-CA

Formal analysis: MWG, WN, M-CA

Investigation: MWG, WN, ER, CM, EvTB, TG, B-CP, SAH, JS, M-CA

Writing – original draft: MWG, M-CA

Writing – Reviewing and editing: MWG, WN, ER, CM, EvTB, TG, B-CP, SAH, JS, M-CA

Funding acquisition: M-CA

Resources: JS, SAH, M-CA

Supervision: M-CA

Competing interests: All authors declare they have no competing interests.

References

1 Brunner, S. *et al.* Gut microbiota restricts intestinal lipid uptake via modulation of bile phosphatidylcholine metabolism in mice. *Nat Microbiol* **11**, 2349–2364 (2026). https://doi.org/10.1038/s41564-026-02434-z

2 Caesar, R., Tremaroli, V., Kovatcheva-Datchary, P., Cani, P. D. & Backhed, F. Crosstalk between Gut Microbiota and Dietary Lipids Aggravates WAT Inflammation through TLR Signaling. *Cell Metab* **22**, 658–668 (2015). https://doi.org/10.1016/j.cmet.2015.07.026

3 Parseus, A. *et al.* Microbiota-induced obesity requires farnesoid X receptor. *Gut* **66**, 429–437 (2017). https://doi.org/10.1136/gutjnl-2015-310283

4 Turnbaugh, P. J. *et al.* An obesity-associated gut microbiome with increased capacity for energy harvest. *Nature* **444**, 1027–1031 (2006). https://doi.org/10.1038/nature05414

5 Tanoue, T. *et al.* Microbiota-mediated induction of beige adipocytes in response to dietary cues. *Nature* **653**, 499–509 (2026). https://doi.org/10.1038/s41586-026-10205-3

6 Duan, S. *et al.* Cross-kingdom nutrient exchange in the plant-arbuscular mycorrhizal fungus-bacterium continuum. *Nat Rev Microbiol* **22**, 773–790 (2024). https://doi.org/10.1038/s41579-024-01073-7

7 Govindarajulu, M. *et al.* Nitrogen transfer in the arbuscular mycorrhizal symbiosis. *Nature* **435**, 819–823 (2005). https://doi.org/10.1038/nature03610
8 Pinto-Tomas, A. A. *et al.* Symbiotic nitrogen fixation in the fungus gardens of leaf-cutter ants. *Science* **326**, 1120–1123 (2009). https://doi.org/10.1126/science.1173036
9 Doron, I. *et al.* Human gut mycobiota tune immunity via CARD9-dependent induction of anti-fungal IgG antibodies. *Cell* **184**, 1017–1031.e1014 (2021). https://doi.org/10.1016/j.cell.2021.01.016
10 Hoskinson, C. *et al.* Saccharomycetes and Malassezia fungi associate with early-life gut maturation and allergic disease risk in childhood. *Nat Commun* **17** (2026). https://doi.org/10.1038/s41467-026-74418-w
11 Huang, H. *et al.* The mycobiome as integral part of the gut microbiome: crucial role of symbiotic fungi in health and disease. *Gut Microbes* **16**, 2440111 (2024). https://doi.org/10.1080/19490976.2024.2440111
12 Nash, A. K. *et al.* The gut mycobiome of the Human Microbiome Project healthy cohort. *Microbiome* **5**, 153 (2017). https://doi.org/10.1186/s40168-017-0373-4
13 van Tilburg Bernardes, E. *et al.* Antibiotic-induced Malassezia expansion in the infant gut promotes early-life immune dysregulation and airway inflammation in mice. *Nat Commun* **17** (2026). https://doi.org/10.1038/s41467-026-74417-x
14 Shao, T. Y. *et al.* Commensal Candida albicans Positively Calibrates Systemic Th17 Immunological Responses. *Cell Host Microbe* **25**, 404–417.e406 (2019). https://doi.org/10.1016/j.chom.2019.02.004
15 Bacher, P. *et al.* Human Anti-fungal Th17 Immunity and Pathology Rely on Cross-Reactivity against Candida albicans. *Cell* **176**, 1340–1355 e1315 (2019). https://doi.org/10.1016/j.cell.2019.01.041
16 Gutierrez, M. W. *et al.* Maturational patterns of the infant gut mycobiome are associated with early-life body mass index. *Cell Rep Med* **4**, 100928 (2023). https://doi.org/10.1016/j.xcrm.2023.100928
17 Gutierrez, M. W. *et al.* Early-life gut mycobiome core species modulate metabolic health in mice. *Nat Commun* **16**, 1467 (2025). https://doi.org/10.1038/s41467-025-56743-8
18 Octoman, A. & Arrieta, M. C. Early-life gut fungi as modulators of metabolic development. *Trends Endocrinol Metab* (2026). https://doi.org/10.1016/j.tem.2026.05.003
19 Co, J. Y. *et al.* Controlling Epithelial Polarity: A Human Enteroid Model for Host-Pathogen Interactions. *Cell Rep* **26**, 2509–2520 e2504 (2019). https://doi.org/10.1016/j.celrep.2019.01.108
20 Martinez-Guryn, K. *et al.* Small Intestine Microbiota Regulate Host Digestive and Absorptive Adaptive Responses to Dietary Lipids. *Cell Host Microbe* **23**, 458–469 e455 (2018). https://doi.org/10.1016/j.chom.2018.03.011
21 Gaudino, S. J. *et al.* Cutting Edge: Intestinal IL-17A Receptor Signaling Specifically Regulates High-Fat Diet-Mediated, Microbiota-Driven Metabolic Disorders. *J Immunol* **207**, 1959–1963 (2021). https://doi.org/10.4049/jimmunol.2000986
22 Pérez, M. M. *et al.* Interleukin-17/interleukin-17 receptor axis elicits intestinal neutrophil migration, restrains gut dysbiosis and lipopolysaccharide translocation in high-fat diet-induced metabolic syndrome model. *Immunology* **156**, 339–355 (2019). https://doi.org/https://doi.org/10.1111/imm.13028

23 Lema, I., Araújo, J. R., Rolhion, N. & Demignot, S. Jejunum: The understudied meeting place of dietary lipids and the microbiota. *Biochimie* **178**, 124–136 (2020). https://doi.org/https://doi.org/10.1016/j.biochi.2020.09.007

24 Chiang, J. Y. Bile acid metabolism and signaling. *Compr Physiol* **3**, 1191–1212 (2013). https://doi.org/10.1002/cphy.c120023

25 Hermankova, E. *et al.* Polymeric bile acid sequestrants: Review of design, in vitro binding activities, and hypocholesterolemic effects. *Eur J Med Chem* **144**, 300–317 (2018). https://doi.org/10.1016/j.ejmech.2017.12.015

26 Keuper, M. & Jastroch, M. The good and the BAT of metabolic sex differences in thermogenic human adipose tissue. *Mol Cell Endocrinol* **533**, 111337 (2021). https://doi.org/10.1016/j.mce.2021.111337

27 Neeland, I. J. *et al.* Visceral and ectopic fat, atherosclerosis, and cardiometabolic disease: a position statement. *Lancet Diabetes Endocrinol* **7**, 715–725 (2019). https://doi.org/10.1016/s2213-8587(19)30084-1

28 Kraunsøe, R. *et al.* Mitochondrial respiration in subcutaneous and visceral adipose tissue from patients with morbid obesity. *J Physiol* **588**, 2023–2032 (2010). https://doi.org/10.1113/jphysiol.2009.184754

29 Trim, W. V. & Lynch, L. Immune and non-immune functions of adipose tissue leukocytes. *Nat Rev Immunol* **22**, 371–386 (2022). https://doi.org/10.1038/s41577-021-00635-7

30 Kohlgruber, A. C. *et al.* γδ T cells producing interleukin-17A regulate adipose regulatory T cell homeostasis and thermogenesis. *Nat Immunol* **19**, 464–474 (2018). https://doi.org/10.1038/s41590-018-0094-2

31 Knights, A. J. *et al.* Eosinophil function in adipose tissue is regulated by Krüppel-like factor 3 (KLF3). *Nature Communications* **11**, 2922 (2020). https://doi.org/10.1038/s41467-020-16758-9

32 Lynch, L. *et al.* iNKT Cells Induce FGF21 for Thermogenesis and Are Required for Maximal Weight Loss in GLP1 Therapy. *Cell Metab* **24**, 510–519 (2016). https://doi.org/10.1016/j.cmet.2016.08.003

33 Brestoff, J. R. *et al.* Group 2 innate lymphoid cells promote beiging of white adipose tissue and limit obesity. *Nature* **519**, 242–246 (2015). https://doi.org/10.1038/nature14115

34 Itohara, S. *et al.* T cell receptor delta gene mutant mice: independent generation of alpha beta T cells and programmed rearrangements of gamma delta TCR genes. *Cell* **72**, 337–348 (1993). https://doi.org/10.1016/0092-8674(93)90112-4

35 Conti, H. R. *et al.* Oral-resident natural Th17 cells and gammadelta T cells control opportunistic Candida albicans infections. *J Exp Med* **211**, 2075–2084 (2014). https://doi.org/10.1084/jem.20130877

36 Chevalier, C. *et al.* Gut Microbiota Orchestrates Energy Homeostasis during Cold. *Cell* **163**, 1360–1374 (2015). https://doi.org/10.1016/j.cell.2015.11.004

37 Lundgren, P. & Thaiss, C. A. The microbiome-adipose tissue axis in systemic metabolism. *Am J Physiol Gastrointest Liver Physiol* **318**, G717–G724 (2020). https://doi.org/10.1152/ajpgi.00304.2019

38 Suarez-Zamorano, N. *et al.* Microbiota depletion promotes browning of white adipose tissue and reduces obesity. *Nat Med* **21**, 1497–1501 (2015). https://doi.org/10.1038/nm.3994

39 Kim, J. Y. *et al.* Obesity-associated improvements in metabolic profile through expansion of adipose tissue. *J Clin Invest* **117**, 2621–2637 (2007). https://doi.org/10.1172/JCI31021

40 Sakers, A., De Siqueira, M. K., Seale, P. & Villanueva, C. J. Adipose-tissue plasticity in health and disease. *Cell* **185**, 419–446 (2022). https://doi.org/10.1016/j.cell.2021.12.016
41 Virtue, S. & Vidal-Puig, A. Adipose tissue expandability, lipotoxicity and the Metabolic Syndrome--an allostatic perspective. *Biochim Biophys Acta* **1801**, 338–349 (2010). https://doi.org/10.1016/j.bbalip.2009.12.006
42 Wahlstrom, A., Sayin, S. I., Marschall, H. U. & Backhed, F. Intestinal Crosstalk between Bile Acids and Microbiota and Its Impact on Host Metabolism. *Cell Metab* **24**, 41–50 (2016). https://doi.org/10.1016/j.cmet.2016.05.005
43 Chen, X. *et al.* Bifidobacterium animalis reshapes the bile acid pool and prevents neonatal jaundice: a clinical microbiome study from correlation to causation. *NPJ Biofilms Microbiomes* (2026). https://doi.org/10.1038/s41522-026-01057-w
44 Fu, Y. *et al.* Blautia coccoides Alleviates Acute Pancreatitis via Bile Salt Hydrolase-mediated Deoxycholic Acid Production and Farnesoid X Receptor Signaling. *Cell Mol Gastroenterol Hepatol* **20**, 101732 (2026). https://doi.org/10.1016/j.jcmgh.2026.101732
45 Lin, Z., Wu, J., Wang, J., Levesque, C. L. & Ma, X. Dietary Lactobacillus reuteri prevent from inflammation mediated apoptosis of liver via improving intestinal microbiota and bile acid metabolism. *Food Chem* **404**, 134643 (2023). https://doi.org/10.1016/j.foodchem.2022.134643
46 Michurina, S. S., Stafeev, I. S., Menshikov, M. Y. & Parfyonova, Y. V. Mitochondrial dynamics keep balance of nutrient combustion in thermogenic adipocytes. *Mitochondrion* **59**, 157–168 (2021). https://doi.org/10.1016/j.mito.2021.05.001
47 Li, X. V. *et al.* Immune regulation by fungal strain diversity in inflammatory bowel disease. *Nature* **603**, 672–678 (2022). https://doi.org/10.1038/s41586-022-04502-w
48 Martini, G. R. *et al.* Antigen-restricted Candida albicans Th17 cells link oral-gut immunity and adopt pathogenic features during intestinal inflammation. *Immunity* (2026). https://doi.org/10.1016/j.immuni.2026.06.013
49 Kim, S. N. *et al.* Sex differences in sympathetic innervation and browning of white adipose tissue of mice. *Biol Sex Differ* **7**, 67 (2016). https://doi.org/10.1186/s13293-016-0121-7
50 Org, E. *et al.* Sex differences and hormonal effects on gut microbiota composition in mice. *Gut Microbes* **7**, 313–322 (2016). https://doi.org/10.1080/19490976.2016.1203502
51 Qin, J. *et al.* A human gut microbial gene catalogue established by metagenomic sequencing. *Nature* **464**, 59–65 (2010). https://doi.org/10.1038/nature08821
52 Peroumal, D., Sahu, S. R., Kumari, P., Utkalaja, B. G. & Acharya, N. Commensal Fungus Candida albicans Maintains a Long-Term Mutualistic Relationship with the Host To Modulate Gut Microbiota and Metabolism. *Microbiol Spectr* **10**, e0246222 (2022). https://doi.org/10.1128/spectrum.02462-22
53 Brugiroux, S. *et al.* Genome-guided design of a defined mouse microbiota that confers colonization resistance against Salmonella enterica serovar Typhimurium. *Nat Microbiol* **2**, 16215 (2016). https://doi.org/10.1038/nmicrobiol.2016.215
54 van Tilburg Bernardes, E. *et al.* Intestinal fungi are causally implicated in microbiome assembly and immune development in mice. *Nature Communications* **11**, 2577 (2020). https://doi.org/10.1038/s41467-020-16431-1
55 Manter, D. K. & Vivanco, J. M. Use of the ITS primers, ITS1F and ITS4, to characterize fungal abundance and diversity in mixed-template samples by qPCR and length heterogeneity analysis. *J Microbiol Methods* **71**, 7–14 (2007). https://doi.org/10.1016/j.mimet.2007.06.016

56 Takahashi, A. *et al.* Post-transcriptional Stabilization of Ucp1 mRNA Protects Mice from Diet-Induced Obesity. *Cell Rep* **13**, 2756–2767 (2015). https://doi.org/10.1016/j.celrep.2015.11.056

57 Caporaso, J. G. *et al.* Ultra-high-throughput microbial community analysis on the Illumina HiSeq and MiSeq platforms. *ISME J* **6**, 1621–1624 (2012). https://doi.org/10.1038/ismej.2012.8

58 Kozich, J. J., Westcott, S. L., Baxter, N. T., Highlander, S. K. & Schloss, P. D. Development of a dual-index sequencing strategy and curation pipeline for analyzing amplicon sequence data on the MiSeq Illumina sequencing platform. *Appl Environ Microbiol* **79**, 5112–5120 (2013). https://doi.org/10.1128/AEM.01043-13

59 Callahan, B. J. *et al.* DADA2: High-resolution sample inference from Illumina amplicon data. *Nat Methods* **13**, 581–583 (2016). https://doi.org/10.1038/nmeth.3869

60 Brown, K. *et al.* Microbiota alters the metabolome in an age- and sex- dependent manner in mice. *Nat Commun* **14**, 1348 (2023). https://doi.org/10.1038/s41467-023-37055-1

61 McMurdie, P. J. & Holmes, S. phyloseq: an R package for reproducible interactive analysis and graphics of microbiome census data. *PLoS One* **8**, e61217 (2013). https://doi.org/10.1371/journal.pone.0061217

62 Schindelin, J. *et al.* Fiji: an open-source platform for biological-image analysis. *Nat Methods* **9**, 676–682 (2012). https://doi.org/10.1038/nmeth.2019

63 Ollion, J., Cochennec, J., Loll, F., Escude, C. & Boudier, T. TANGO: a generic tool for high-throughput 3D image analysis for studying nuclear organization. *Bioinformatics* **29**, 1840–1841 (2013). https://doi.org/10.1093/bioinformatics/btt276

64 Agrawal, S. *et al.* El-MAVEN: A Fast, Robust, and User-Friendly Mass Spectrometry Data Processing Engine for Metabolomics. *Methods Mol Biol* **1978**, 301–321 (2019). https://doi.org/10.1007/978-1-4939-9236-2_19

65 Mu, C. & Shearer, J. Protocol for measuring respiratory function of mitochondria in frozen colon tissue from rats. *STAR Protoc* **4**, 102560 (2023). https://doi.org/10.1016/j.xpro.2023.102560

66 Sahl, R. E. *et al.* Reliability and variation in mitochondrial respiration in human adipose tissue. *Adipocyte* **10**, 605–611 (2021). https://doi.org/10.1080/21623945.2021.1991617

67 Chung, K. J. *et al.* A self-sustained loop of inflammation-driven inhibition of beige adipogenesis in obesity. *Nat Immunol* **18**, 654–664 (2017). https://doi.org/10.1038/ni.3728

68 Lee, A. H. & Dixit, V. D. Dietary Regulation of Immunity. *Immunity* **53**, 510–523 (2020). https://doi.org/10.1016/j.immuni.2020.08.013

69 Kane, H. & Lynch, L. Innate Immune Control of Adipose Tissue Homeostasis. *Trends Immunol* **40**, 857–872 (2019). https://doi.org/10.1016/j.it.2019.07.006

70 vegan: Community Ecology Package v. 2.5-7 (R package, 2020).

71 Love, M. I., Huber, W. & Anders, S. Moderated estimation of fold change and dispersion for RNA-seq data with DESeq2. *Genome Biol* **15**, 550 (2014). https://doi.org/10.1186/s13059-014-0550-8

Main figures

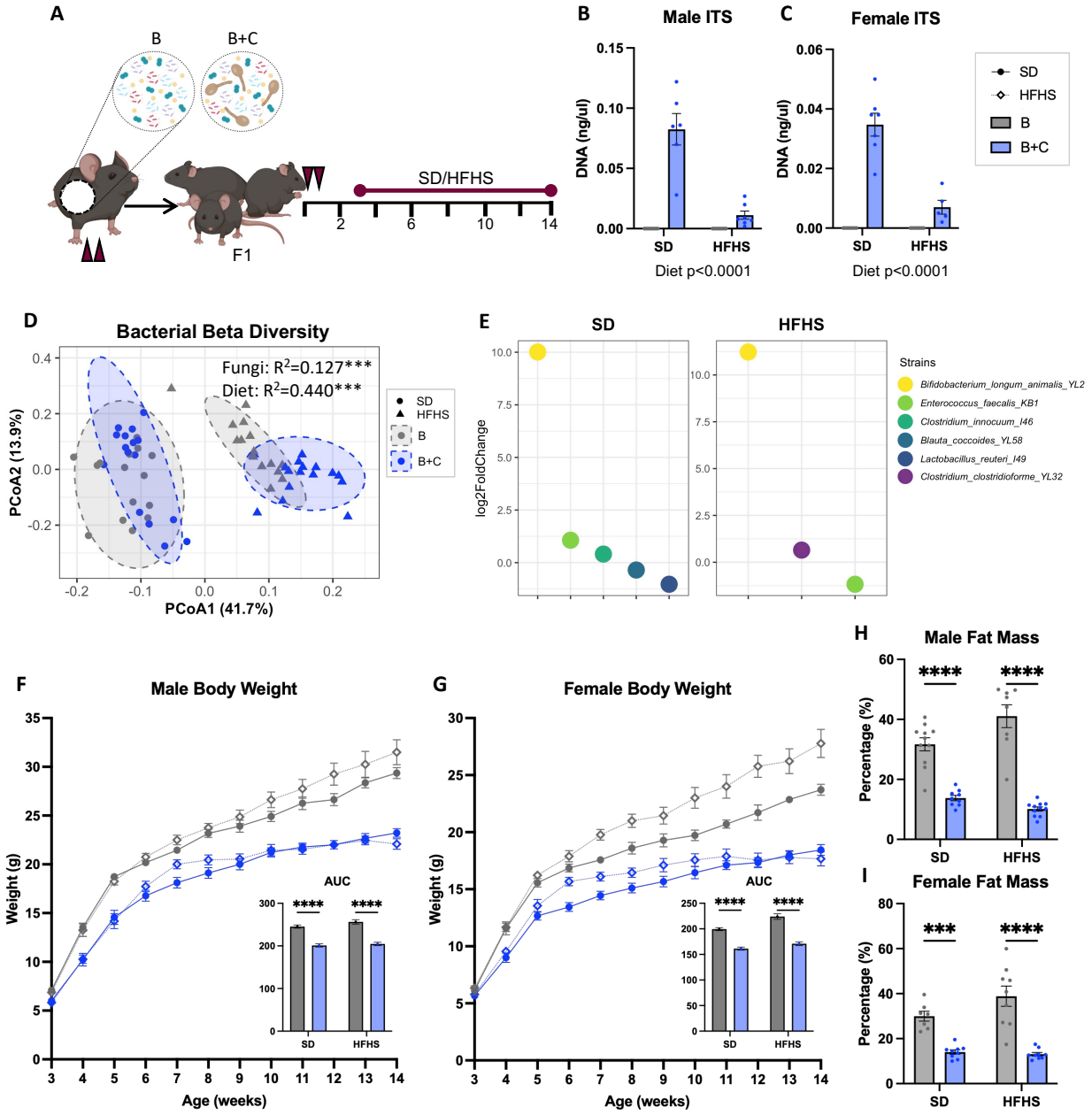


Figure 1. Early-life colonization with *C. albicans* shifts the bacterial microbiome and reduces body weight and fat mass.

A) Gnotobiotic colonization and DIO model. GF dams were gavaged twice with Oligo-MM12 consortium alone ("B") or in combination with *C. albicans* ("B+C"). B+C offspring (F1) were further exposed to *C. albicans* twice in the first week of life. F1 were weaned onto standard diet (SD) or high-fat-high-sucrose diet (HFHS) until 14 weeks of age. **B-C**) Fecal ITS DNA at 14 weeks in males and females. **D)** Principal coordinate analysis (PCoA) plots of bacterial beta-diversity at 12 weeks. Fungi and diet effect based on Bray-Curtis Dissimilarity assessed by PERMANOVA. Ellipses represent 95% confidence intervals (CI). **E)** Bacterial differential abundance using DESeq2. Log_2 fold changes represent differences in abundance between groups

(B+C vs B), with positive values indicating enrichment in the B+C group. P-values were adjusted for multiple testing using the Benjamini–Hochberg method, and taxa with adjusted $p < 0.05$ are shown. **F-G**) Body weight from 3-14 weeks with trapezoidal AUC in males and females. **H-I**) Fat mass percentage in males and females, respectively. Statistical significance defined by two-way ANOVA with Šídák's multiple comparisons test. Data represented as mean ± SEM. *$p < 0.05$, **$p < 0.01$, ***$p < 0.001$, ****$p < 0.0001$.

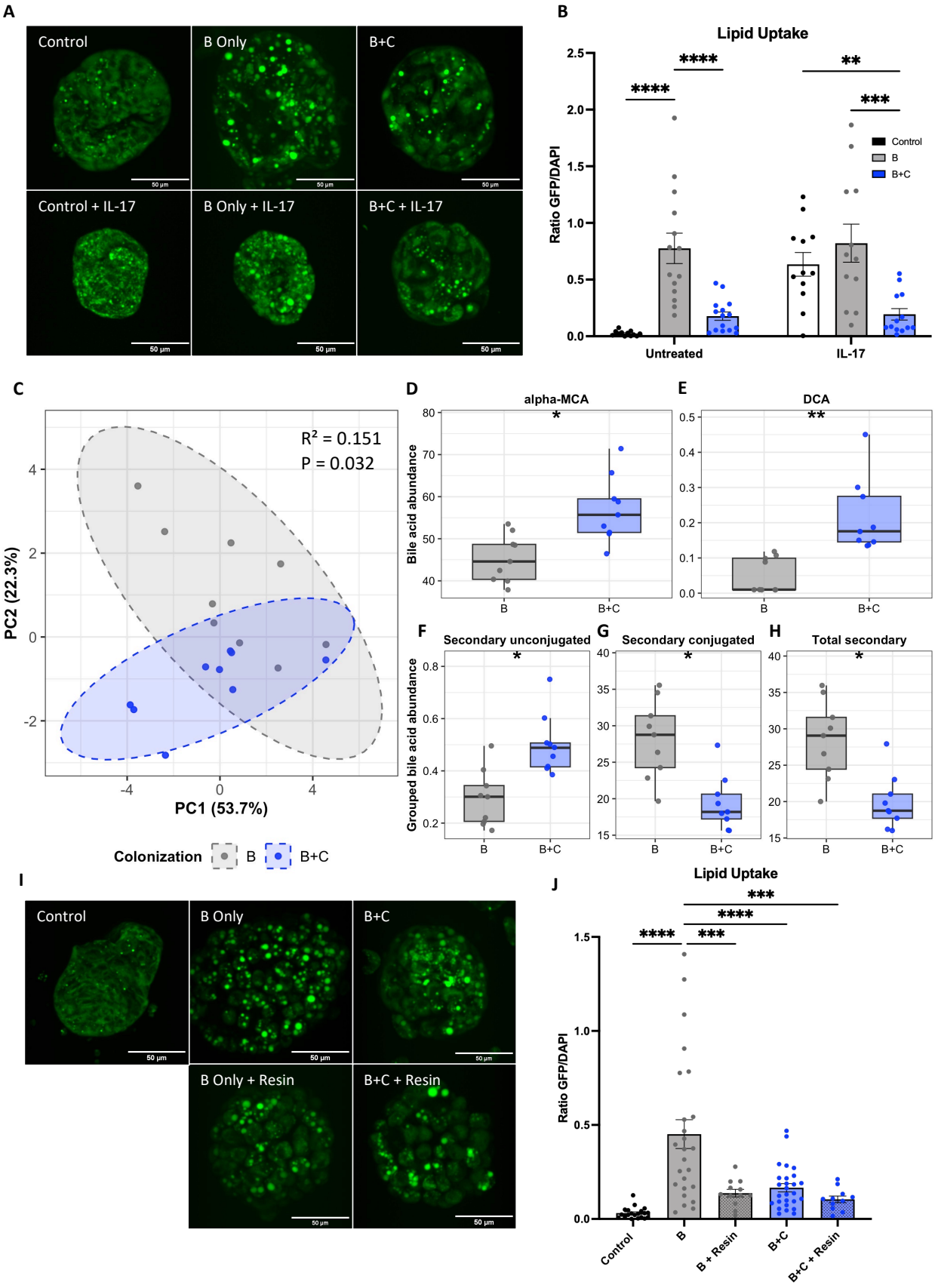

A
Control
B Only
B+C
Control + IL-17
B Only + IL-17
B+C + IL-17
50 µm
B
Lipid Uptake
Ratio GFP/DAPI
Control
B
B+C
Untreated
IL-17
****
****
**
***
C
R² = 0.151
P = 0.032
PC2 (22.3%)
PC1 (53.7%)
Colonization
B
B+C
D
alpha-MCA
Bile acid abundance
E
DCA
F
Secondary unconjugated
Grouped bile acid abundance
G
Secondary conjugated
H
Total secondary
I
Control
B Only
B+C
B Only + Resin
B+C + Resin
J
Lipid Uptake
Ratio GFP/DAPI
Control
B
B + Resin
B+C
B+C + Resin

Figure 2. *C. albicans* colonization remodels the bile acid landscape and impairs intestinal lipid uptake

A) Representative images of inverted jejunal enteroids exposed to sterile fecal filtrates from mice colonized with the Oligo-MM12 bacterial consortium alone (B only) or with *C. albicans* (B+C) in the presence or absence of IL-17 and oleic acid. Lipid droplets stained with BODIPY AF488. **B**) Quantification of jejunal enteroid lipid uptake expressed as BODIPY fluorescence volume normalized to DAPI signal volume. Statistical comparisons performed by two-way ANOVA, Untreated: Control n=15, B n=14, B+C n=15; IL-17: Control n=13, B n=12, B+C n= 13, ***p*<0,01, ****p*<0,001, *****p*<0.0001. **C**) Principal component analysis (PCA) of log-transformed, scaled bile acid concentrations from B and B+C mice. Group separation was assessed by PERMANOVA. Ellipses represent 95% CI. **D-E**) Individual and (**F-H**) grouped bile acid concentrations. Boxplots indicate median and interquartile range, with whiskers representing 1.5× IQR. Statistical comparisons between groups were performed using two-sided Mann–Whitney U tests with Benjamini–Hochberg false discovery rate (FDR) correction. Significance is indicated as *FDR < 0.05, **FDR < 0.01. **I**) Representative images of jejunal enteroids exposed to sterile fecal filtrates from B or B+C mice in the presence or absence of bile acid sequestrant resin, cholestyramine. Lipid droplets stained with BODIPY AF488. **J**) Quantification of jejunal enteroid lipid uptake following cholestyramine treatment, expressed as BODIPY fluorescence volume (GFP) normalized to DAPI signal volume. Statistical comparisons performed by one-way ANOVA, Control n=26, B Only n=26, B Only + Resin n=12, B+C n=27, B+C + Resin n=11, ****p*<0.001, *****p*<0.0001.

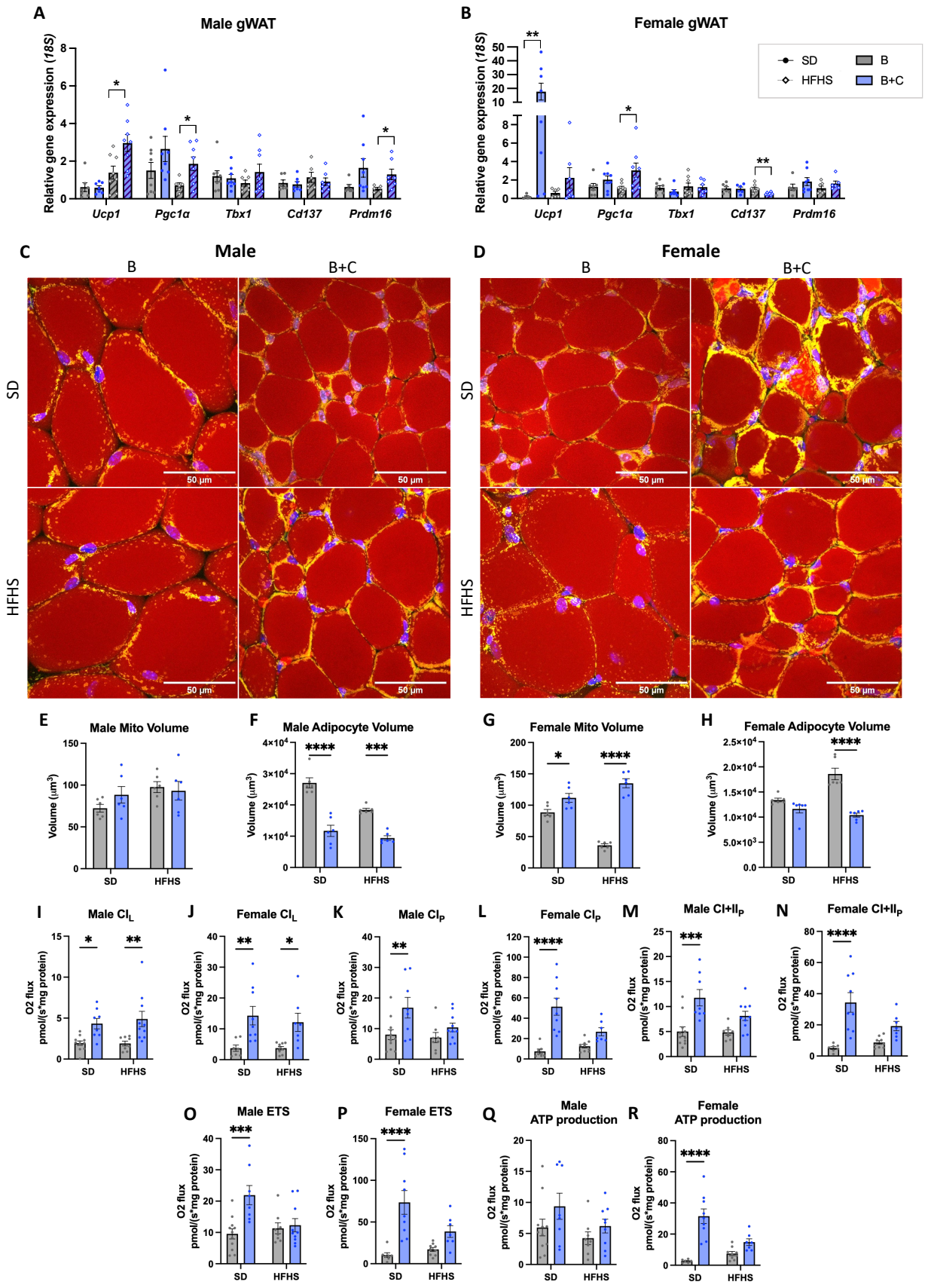

A
Male gWAT
Relative gene expression (18S)
Ucp1
Pgc1α
Tbx1
Cd137
Prdm16
B
Female gWAT
SD
HFHS
B
B+C
C
Male
D
Female
B
B+C
SD
HFHS
50 µm
E
Male Mito Volume
F
Male Adipocyte Volume
G
Female Mito Volume
H
Female Adipocyte Volume
Volume (µm³)
I
Male CI_L
J
Female CI_L
K
Male CI_P
L
Female CI_P
M
Male CI+II_P
N
Female CI+II_P
O2 flux pmol/(s*mg protein)
O
Male ETS
P
Female ETS
Q
Male ATP production
R
Female ATP production

Figure 3. *C. albicans* colonization enhances thermogenic programming and mitochondrial density in white adipose tissue.

A-B) Relative gene expression normalized to *18S* (calculated using $2^{-\Delta\Delta Ct}$) of thermogenesis-associated genes in peri-gonadal white adipose tissue (WAT), in males **(A)** and females **(B)** fed a SD (solid bars) or a HFHS diet (striped bars). Statistical significance within each diet was determined using an unpaired *t*-test or Mann–Whitney *U* test following assessment of normality by the Shapiro–Wilk test. **C-D**) Representative immunofluorescence images of gWAT from male **(C)** and female **(D)** mice. Adipocytes autofluorescence was quenched with Sudan Black (red), mitochondria were labeled with TOMM20 (yellow), and nuclei with DAPI (blue). **E-H**) Quantification of mitochondrial (**E, G**) and adipocyte (**F, H**) volume in males and females. **I–T)** High-resolution respirometry of gWAT mitochondria from male and female mice. **I-J**) Complex I leak respiration (CI_L) in males and females. **K-L**) Complex I linked respiration (CI_P) in males and females. **M-N**) Complex I+II linked respiration ($CI+II_P$) in males and females. **O-P)** Maximum electron transport system respiration (ETS) in males and females. **Q-R**) ATP production in males and females. For panels E-R, Statistical differences defined by Two-way ANOVA with Šídák's multiple comparisons test. Data represented as mean ± SEM. *$p < 0.05$, **$p < 0.01$, ***$p < 0.001$, ****$p < 0.0001$.

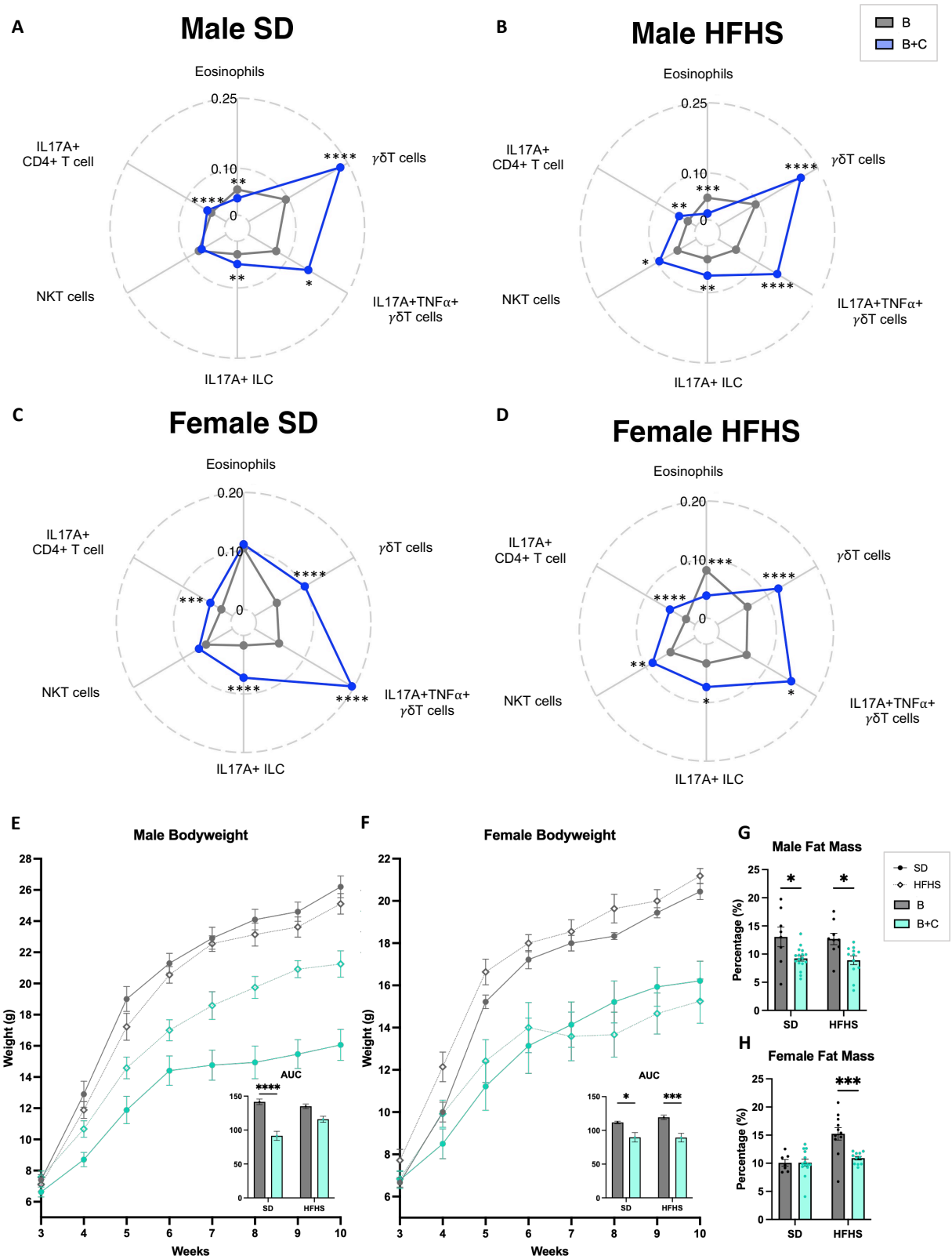


Figure 4. γδT cells in WAT contribute to the lean phenotype induced by *C. albicans* colonization

A-D) Radar plots showing the proportion of adipose-resident immune cell populations quantified by flow cytometry in gWAT from male (**A–B**) and female (**C–D**) mice fed a standard diet (SD) or high-fat high-sucrose diet (HFHS). Cell populations include those previously shown to have pro-thermogenic function: eosinophils, γδ T cells, IL-17A$^+$TNF-α$^+$ γδ T cells, IL-17A$^+$ innate lymphoid cells (ILCs), natural killer T (NKT) cells, and IL-17A$^+$CD4$^+$ T cells. Values represent the proportion of each immune cell population within the CD45$^+$ leukocyte compartment. Statistical comparisons between B and B+C mice were performed using unpaired *t*-tests. **E-F**) Body weight trajectories of gnotobiotic γδT cell deficient mice colonized with the Oligo-MM12 consortium alone (B) or together with *C. albicans* (B+C), fed either SD or HFHS. Inserts show the area under the curve (AUC) for body weight from 3–10 weeks of age. **G-H**) Body fat percentage of γδTCR-deficient mice following SD or HFHS feeding in males (**G**) and females (**H**). For panels E-H, statistical significance was determined by two-way ANOVA with Šídák's multiple comparisons test. Data represented as mean ± SEM. *$p < 0.05$, **$p < 0.01$, ***$p < 0.001$, ****$p < 0.0001$.

Supplementary Files

This is a list of supplementary files associated with this preprint. Click to download.

- candidametabolismsuppSep6.pdf